

# TRIANGULATION OF SPACE-BASED OPTICAL MEASUREMENTS FOR IMPROVED SPACE SURVEILLANCE AND TRACKING

Annarita Argirò<sup>(1)</sup>, Giorgio Isoletta<sup>(1)</sup>, Roberto Opromolla<sup>(1)</sup>, Giancarmine Fasano<sup>(1)</sup>

<sup>(1)</sup>, Department of Industrial Engineering, University of Naples "Federico II", Piazzale V. Tecchio 80, 80125 Naples, Italy, Email: [annarita.argiro@unina.it](mailto:annarita.argiro@unina.it), [giorgio.isoletta@unina.it](mailto:giorgio.isoletta@unina.it), [roberto.opromolla@unina.it](mailto:roberto.opromolla@unina.it), [g.fasano@unina.it](mailto:g.fasano@unina.it).

## ABSTRACT

The increasing number of Resident Space Objects (RSOs) threatens the safety of satellites and the long-term sustainability of space activities. Current RSOs monitoring relies mainly on ground-based instruments, but space-based sensors offer significant advantages, including higher observation frequency and independence from weather and geographical constraints. This work investigates the feasibility of using space-based optical sensors to determine the 3D position of RSOs by means of triangulation methods. Within the framework of Initial Orbit Determination (IOD), the obtained range information allows transforming the angles-only IOD into a three-dimensional vector-based one, thus improving accuracy. A sensitivity analysis is conducted to evaluate how the different configurations of the space-based sensors with respect to the observed RSO, and the non-idealities of the measurement process, affect the accuracy of range and orbit determination. The analysis is conducted on synthetic test cases exploiting realistic simulations that takes into account RSO detectability.

## 1 INTRODUCTION

From the first space launch in 1957 to date, the number of Resident Space Objects (RSOs) is increased sharply especially due to the occurrence of on-orbit fragmentation events and for launches of mega-constellations of satellites. Currently, about 35 000 objects are tracked by space surveillance networks, about 9 100 of which are active payloads, while the other 26 000 are pieces of debris larger than 10 cm [1]. Within an increasingly crowded space environment, the capability to detect, catalogue and track RSOs becomes more and more critical to ensure safe and sustainable space operations.

The current knowledge of the RSOs is mainly based on ground-based instruments including telescopes, radar and laser systems. However, ground-based sensors have several limitations. First, ground-based observations are limited by geographical constraints, as they require widely distributed ground stations to observe as many space objects as possible [2]. Furthermore, ground-based telescopes cannot operate continuously since their measurements are interrupted by daylight and cloud coverage, besides being affected by atmospheric effects

such as scattering, diffractions, aberrations and turbulences [3]. To go beyond these limitations, space-based sensors have emerged as a promising alternative, being able to offer clearer and more frequent observations than their terrestrial counterparts. In the last decades, several demonstration missions such as the Midcourse Space Experiment (MSX)/Space-Based Visible (SBV) [4], the SBSS 10 Block [5], and Sapphire [6] have been launched to leverage the advantages of space-based RSOs monitoring. The above-mentioned Space Based Space Surveillance (SBSS) programmes are based on passive optical sensors. Indeed, compared to radar and laser systems, optical sensors have smaller size and lower power requirements, making them the preferred technology for space-based RSOs observation [7]. Although a single optical sensor only provides angular measurements, simultaneous observations provided by two or more optical sensors can be used to determine the range and, thus, the 3D position of space debris by means of triangulation methods [8]. Several works address the problem of triangulating angles-only measurements to determine the range information [8, 9, 10, 11]. While Ref. [8], [9] and [10] have proposed triangulation algorithms when dealing with ground-based observations, Hussain et al. [7] applied the triangulation method proposed by Sanders-Reed [11] for RSOs tracking considering both ground-based and space-based optical sensors. However, triangulation can be useful for several purposes, including the improvement of the accuracy of initial orbit determination (IOD), which is of paramount importance for the cataloguing of space debris. Indeed, when dealing with space-based observations, the results of the angles-only IOD generally have large errors, especially if the observed arcs are too short and lack range information. Therefore, based on triangulation with two optical sensors, the angles-only IOD problem can be converted to IOD using 3D position data, thus significantly improving IOD accuracy.

These techniques can be useful in different application frameworks, including the concept of distributed space systems with large baselines (hundreds of kilometres) for space-based SSA. Indeed, when avoiding too large separations between the sensors, they would be able to observe the same object under similar illumination conditions, overcoming detection limitations and enabling simultaneous observations. At the same time, the spatial diversity provided by sensors separation

would enable accurate triangulation and thus precise range estimation, effectively supporting orbit determination, especially for Low Earth Orbit (LEO) to LEO observation scenarios.

Within this framework, this work investigates the feasibility of triangulating angle-only measurements provided by space-based optical sensors to estimate the 3D position of an RSO of interest. Specifically, in this work, the triangulation method developed by Sanders-Reed [11] has been applied to determine the range information in order to improve the IOD accuracy. This method has previously been applied in the literature for RSOs tracking, but without taking into account any detectability conditions. Therefore, in this work, observability constraints have been introduced to identify the actual observation windows, allowing for a more realistic assessment of the applicability of the proposed methodology. A sensitivity analysis is conducted to evaluate how different configurations of space-based sensors with respect to the observed RSO and measurement uncertainties affect the accuracy of range and orbit determination. The remainder of the paper is organised as follows. Section 2 provides a description of the proposed triangulation methodology and its implementation within an IOD architecture. Section 3 presents and discusses the results obtained applying the proposed methodology to synthetic test cases. Section 4 draws some conclusions and provides indication about potential future works.

## 2 METHODOLOGY

The proposed methodology is described in Fig. 1.

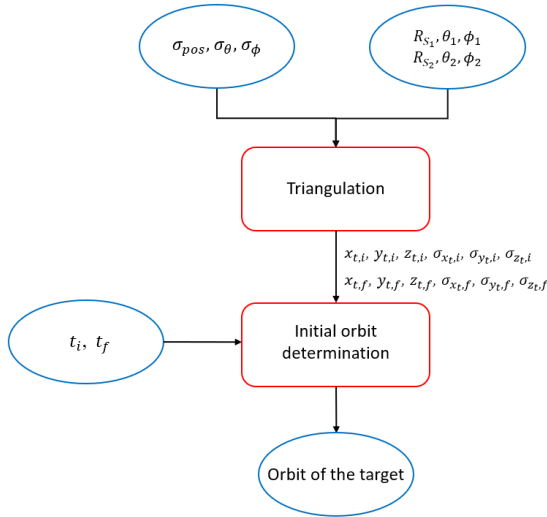


Figure 1. Workflow of the proposed methodology.

As shown in Fig. 1, the positions vectors of two space-based optical sensors,  $R_{S_1}$  and  $R_{S_2}$ , and the angular measurements  $(\theta_1, \phi_1)$  and  $(\theta_2, \phi_2)$  provided by the first and second sensor, respectively, are required to

perform triangulation. In addition, it is necessary to know the uncertainties on the sensor positions  $\sigma_{pos}$  and on the angular measurements  $\sigma_\theta$  and  $\sigma_\phi$ , assuming that they are the same for both sensors. The  $R_{S_1}, \theta_1, \phi_1$  and  $R_{S_2}, \theta_2, \phi_2$  are defined as described in subsection 2.1. Moreover, it should be underlined that  $R_{S_1}, \theta_1, \phi_1$  and  $R_{S_2}, \theta_2, \phi_2$  are given during the observation windows, which are obtained by propagating under Keplerian assumption the two sensors and target (i.e., the RSO of interest) and taking into account the observation constraints described in subsection 2.2. Therefore, starting from  $R_{S_1}, \theta_1, \phi_1$  and  $R_{S_2}, \theta_2, \phi_2$  during the observation windows and  $\sigma_{pos}, \sigma_\theta$  and  $\sigma_\phi$ , a state-of-the-art triangulation method is applied to determine the 3D position of the target, i.e.,  $x_t, y_t$ , and  $z_t$ , as well as the estimates of the uncertainties for the x, y and z components, i.e.,  $\sigma_{x_t}, \sigma_{y_t}$  and  $\sigma_{z_t}$ . A description of the applied triangulation method is given in subsection 2.3. The two position vectors of the target at the beginning and end of the observation window showing the lowest estimation errors, together with the corresponding epochs, enable to determine the orbit of the target by solving the Lambert's problem (see subsection 2.4).

### 2.1 Problem statement

In the Earth Centred Inertial (ECI) reference frame,  $T$  denotes the target and  $S$  denotes the satellite carrying the optical sensor, as illustrated in Fig. 2. Therefore,  $\underline{R}_{T,ECI}$  and  $\underline{R}_{S,ECI}$  are the vectors that identify the positions of the target and the sensor, respectively, in the ECI reference frame.

Both the sensor and target dynamics are described by the two-body equation of motion (Eq. 1).

$$\ddot{\underline{R}} + \frac{\mu}{R^3} \underline{R} = 0 \quad (1)$$

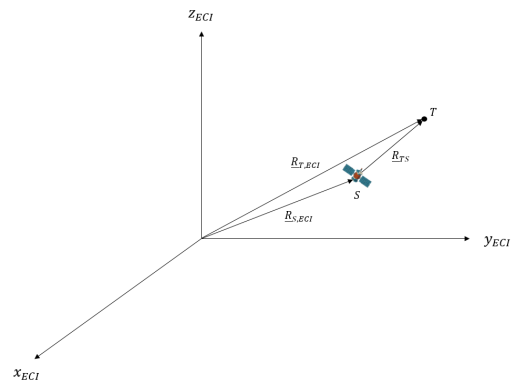


Figure 2. Sensor and target in the ECI reference frame.

As depicted in Fig. 3,  $\underline{R}_{TS}$  is the position vector that identifies the target in a reference frame with origin in the

sensor and with axes parallel to those of the ECI reference frame. In particular,  $\underline{R}_{TS}$  is computed as shown in Eq. 2.

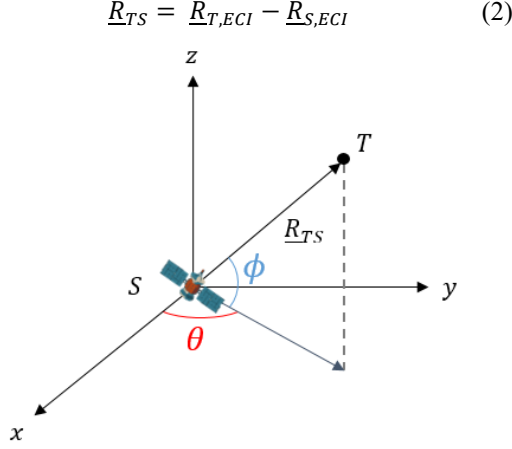


Figure 3. Optical sensor measurements in the sensor-centred reference frame.

The two angular measurements that identify the position of the target in the sensor-centred reference frame are the right ascension  $\theta$  and the declination  $\phi$ , which are defined as in Eqs. 3-4.

$$\theta = \tan^{-1}\left(\frac{R_{TS,y}}{R_{TS,x}}\right) \quad (3)$$

$$\phi = \tan^{-1}\left(\frac{R_{TS,z}}{\sqrt{R_{TS,x}^2 + R_{TS,y}^2}}\right) \quad (4)$$

where  $R_{TS,x}, R_{TS,y}, R_{TS,z}$  are the components of the position vector  $\underline{R}_{TS}$  along the axes of the sensor-centred reference frame.

## 2.2 Observation constraints

The target can be detected by an optical sensor only when some observation constraints are met. Specifically, they take into account the capability of the sensor to track the target, the Earth's shadow, the Sun illumination, the presence of the Earth in the background and the target's visual magnitude.

First, the target can be observed if the sensor is able to track it. To this purpose, the angle  $\alpha_j$  between two consecutive unit vector from the sensor to the target, i.e.,  $\hat{R}_{TS,j}$  and  $\hat{R}_{TS,j+1}$ , has to be computed according to Eq. 5 for  $j = 1, \dots, N_{T-1} - 1$  with  $N_{T-1}$  being the number of time instants.

$$\alpha_j = \cos^{-1}\left(\frac{\hat{R}_{TS,j} \cdot \hat{R}_{TS,j+1}}{\|\hat{R}_{TS,j}\| \cdot \|\hat{R}_{TS,j+1}\|}\right) \quad (5)$$

After that, if  $|\alpha_j| > \frac{FOV}{2}$ , where FOV denotes the field of view of the sensor, the slew angle  $\delta_j$  is calculated according to Eq. 6.

$$\delta_j = \begin{cases} \alpha_j + \frac{FOV}{2} & \text{if } \alpha_j < 0 \\ \alpha_j - \frac{FOV}{2} & \text{if } \alpha_j > 0 \end{cases} \quad (6)$$

Assuming a maximum slew rate of  $\omega_{slew,max} = 0.5^\circ/s$ , the sensor can track the target if the condition given in Eq. 7 is fulfilled, being  $t_{step}$  the time step between two consecutive time instants.

$$|\delta_j| < \delta_{max} = \omega_{slew,max} \cdot t_{step} \quad (7)$$

The second condition to be considered is the presence of the Sun in the sensor's FOV, as the sensor cannot work when dazzled by sunlight. Thus, denoting  $\hat{R}_{sun,ECI}$  as the unit vector that identifies the position of the Sun in the ECI reference frame and assuming that the sensor is aligned with  $\hat{R}_{TS}$ , this constraint is defined by Eq. 8.

$$\hat{R}_{TS} \cdot \hat{R}_{sun,ECI} < \cos\left(\frac{FOV}{2}\right) \quad (8)$$

Third, the target can be observed by the sensor when it is outside the Earth's shadow. Thus, being  $R_{Earth}$  the mean radius of the Earth, this condition can be analytically expressed as shown in Eq. 9 [12].

$$\|\underline{R}_{T,ECI} \times \hat{R}_{sun,ECI}\| > R_{Earth} \quad (9)$$

The fourth condition states that the target is visible to the sensor when the Earth is not in the observation background. This condition can be analytically expressed as given in Eq. 10.

$$\|\underline{R}_{S,ECI} \times \hat{R}_{T,ECI}\| < R_{Earth} \quad (10)$$

Finally, the target can be observed by the sensor when its visual magnitude is less than the maximum visual magnitude detectable by the sensor, as shown in Eq. 11. In particular, Eq. 11 is applied considering  $m_{v,max} = 15$ ,

using as a reference the detector of the Sapphire satellite which is capable of monitoring and tracking objects with a magnitude as faint as 15 [6].

$$m_v < m_{v,max} \quad (11)$$

The visual magnitude  $m_v$  is calculated using Eq. 12, under the assumption of a spherical target [13].

$$m_v = m_{v,ref} - 2.5 \log_{10} \left[ \frac{d^2}{R_{TS}^2} \left( \frac{\rho_{spec}}{4} + \rho_{diff} p_{diff}(\psi) \right) \right] \quad (12)$$

In Eq. 12,  $m_{v,ref}$  is a reference value for the visual magnitude assumed to be that of the Sun ( $m_{v,ref} = -26.7$ ),  $d$  is the diameter of the spherical target,  $\rho_{spec}$  and  $\rho_{diff}$  are respectively the specular and diffuse reflection components of the surface of the observed object, and  $p_{diff}$  is a function of the phase angle  $\psi$ , which is defined as the angle between the direction from the target to the Sun and the direction from the target to the sensor. For a diffuse sphere,  $p_{diff}$  is computed according to Eq. 13 [13].

$$p_{diff}(\psi) = \frac{2}{3\pi} [\sin \psi + (\pi - \psi) \cos \psi] \quad (13)$$

### 2.3 Triangulation

A single optical sensor only provides angles measurements, which are insufficient to determine the range information. To this aim, two or more optical sensors can be used to determine the range and thus the 3D position of an object by simple triangulation [7]. A schematic representation of the triangulation problem is shown in Fig. 4.

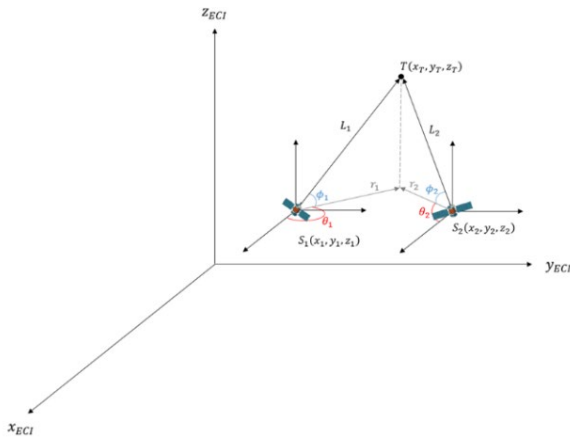


Figure 4. Representation of the triangulation problem.

The 3D positions of the two sensors  $S_1(x_1, y_1, z_1)$  and  $S_2(x_2, y_2, z_2)$  in the ECI reference frame, along with the right ascension and declination measurements  $(\theta_1, \phi_1)$  and  $(\theta_2, \phi_2)$  provided by sensors  $S_1$  and  $S_2$ , respectively, enable to determine the 3D position of the target  $T(x_t, y_t, z_t)$  in the ECI reference frame. The  $x_t$ ,  $y_t$  and  $z_t$  coordinates of the target are computed according to Eqs. 14-16 [14].

$$x_t = \frac{x_1 \tan \theta_1 - x_2 \tan \theta_2 + y_2 - y_1}{\tan \theta_1 - \tan \theta_2} \quad (14)$$

$$y_t = \frac{y_2 \tan \theta_1 - y_1 \tan \theta_2 + (x_1 - x_2) \tan \theta_1 \tan \theta_2}{\tan \theta_1 - \tan \theta_2} \quad (15)$$

$$z_t = \frac{r_1 \tan \phi_1 + z_1 + r_2 \tan \phi_2 + z_2}{2} \quad (16)$$

In Eq. 16,  $r_1$  and  $r_2$ , which are the projection in the  $xy$  plane of the ECI reference frame of the line of sight from the first and second sensor to the target, respectively, are computed according to Eq. 17 [14].

$$r_i = \sqrt{(x_i - x_t)^2 + (y_i - y_t)^2}, i = 1, 2 \quad (17)$$

The error propagation equations that relate the standard deviation of measurement errors to errors in the final target location estimation are derived in [14] under the assumption that the error generated by each sensor follows a Gaussian distribution. The estimates of the standard deviation of  $x_t$ ,  $y_t$ ,  $r_i$  and  $z_t$  are given in Eqs. 18-21, assuming that the standard deviations of the measurement errors of sensors 1 and 2 are equal to each other and that the measurement errors of the sensor position have the same standard deviations in the  $x$ - and  $y$ -direction.

$$\sigma_{x_t} \approx \left\{ \left[ \left( \frac{\partial x_t}{\partial x_1} \right)^2 + \left( \frac{\partial x_t}{\partial x_2} \right)^2 + \left( \frac{\partial x_t}{\partial y_1} \right)^2 + \left( \frac{\partial x_t}{\partial y_2} \right)^2 \right] \sigma_{pos}^2 + \left[ \left( \frac{\partial x_t}{\partial \theta_1} \right)^2 + \left( \frac{\partial x_t}{\partial \theta_2} \right)^2 \right] \sigma_{\theta}^2 \right\}^{1/2} \quad (18)$$

$$\sigma_{y_t} \approx \left\{ \left[ \left( \frac{\partial y_t}{\partial x_1} \right)^2 + \left( \frac{\partial y_t}{\partial x_2} \right)^2 + \left( \frac{\partial y_t}{\partial y_1} \right)^2 + \left( \frac{\partial y_t}{\partial y_2} \right)^2 \right] \sigma_{pos}^2 + \left[ \left( \frac{\partial y_t}{\partial \theta_1} \right)^2 + \left( \frac{\partial y_t}{\partial \theta_2} \right)^2 \right] \sigma_{\theta}^2 \right\}^{1/2} \quad (19)$$

$$\sigma_{r_i}^2 \approx \left\{ \left( \frac{\partial r_i}{\partial x_i} \right)^2 + \left( \frac{\partial r_i}{\partial y_i} \right)^2 + \left( \frac{\partial r_i}{\partial x_t} \right)^2 \left[ \left( \frac{\partial x_t}{\partial x_1} \right)^2 + \left( \frac{\partial x_t}{\partial x_2} \right)^2 + \left( \frac{\partial x_t}{\partial y_1} \right)^2 + \left( \frac{\partial x_t}{\partial y_2} \right)^2 \right] + \left( \frac{\partial r_i}{\partial y_t} \right)^2 \left[ \left( \frac{\partial y_t}{\partial x_1} \right)^2 + \left( \frac{\partial y_t}{\partial x_2} \right)^2 + \right. \right. \quad (20)$$

$$\begin{aligned} & \left. \left( \frac{\partial y_t}{\partial y_1} \right)^2 + \left( \frac{\partial y_t}{\partial y_2} \right)^2 \right\} \sigma_{pos}^2 + \\ & \left\{ \left( \frac{\partial r_i}{\partial x_t} \right)^2 \left[ \left( \frac{\partial x_t}{\partial \theta_1} \right)^2 + \left( \frac{\partial x_t}{\partial \theta_2} \right)^2 \right] + \right. \\ & \left. \left( \frac{\partial r_i}{\partial y_t} \right)^2 \left[ \left( \frac{\partial y_t}{\partial \theta_1} \right)^2 + \left( \frac{\partial y_t}{\partial \theta_2} \right)^2 \right] \right\} \sigma_\theta^2 \\ \sigma_{z_t} & \approx \left[ \left( \frac{\partial z_t}{\partial r_i} \right)^2 \sigma_{r_i}^2 + \left( \frac{\partial z_t}{\partial \phi_i} \right)^2 \sigma_{\phi_i}^2 + \sigma_{z_i}^2 \right]^{1/2} \quad (21) \end{aligned}$$

In Eqs. 18-21,  $\sigma_{pos}$  is the standard deviation in the position measurement,  $\sigma_\theta$  is the standard deviation in the right ascension measurement and  $\sigma_\phi$  is the standard deviation in the declination measurement.

Eq. 21 provides the standard deviation of  $z_T$  considering a single sensor. Since the determination of the 3D position of a target is performed by triangulating the angles-only measurements provided by two sensors, the error estimate for the  $z_T$  can be computed according to Eq. 22 [14].

$$\begin{aligned} \langle \sigma_{z_t} \rangle & \approx \frac{1}{2} \left[ \sigma_{z_t}^2(1) + \sigma_{z_t}^2(2) + \right. \\ & \left. 2 \frac{\partial z_t}{\partial r_1} \frac{\partial z_t}{\partial r_2} \text{Cov}(\delta r_1, \delta r_2) \right]^{1/2} \quad (22) \end{aligned}$$

In Eq. 22,  $\sigma_{z_t}(1)$  and  $\sigma_{z_t}(2)$  are obtained from Eq. 21 for sensor 1 and sensor 2, respectively, while  $\text{Cov}(\delta r_1, \delta r_2) = \frac{\partial r_1}{\partial x_t} \frac{\partial r_2}{\partial x_t} \sigma_{x_t}^2 + \frac{\partial r_1}{\partial y_t} \frac{\partial r_2}{\partial y_t} \sigma_{y_t}^2$ .

It should be pointed out that the optimal geometry for a two-sensor system is to have a  $90^\circ$  separation angle between the two sensors with a  $0^\circ$  elevation angle. In particular,  $\sigma_{x_t}$ ,  $\sigma_{y_t}$  and  $\sigma_{z_T}$  begin to increase rapidly when the separation angle drops to less than  $40^\circ$  [11].

## 2.4 Initial orbit determination

In the literature, there are several approaches to address the IOD problem when the range information is available. Among them, the Gibbs [15] and Herrick-Gibbs [16] methods stand out, which require knowledge of three position vectors along with the time of the measurements. Specifically, the Gibbs method requires the knowledge of three nonzero, coplanar position vectors, which represent three time-sequential vectors of a satellite in its orbit. However, its accuracy significantly degrades when the position vectors are closely spaced, making the solution unreliable. To address this limitation, the Herrick-Gibbs method introduces a Taylor-series expansion to obtain an expression for the middle velocity vector, improving accuracy when the position vectors are relatively close together [12]. Other approaches enable to solve the IOD problem using only two position vectors with their corresponding time instants in a Lambert's formulation.

There are several solutions to Lambert's problem in literature, including Lambert's original geometric formulation [17], the original Gauss formulation [18], the Battin's method [19], Gooding's algorithm [20] and Thorne's solution [21]. In this paper, the orbit of the target is determined by solving the Lambert's problem using the Battin's method, which is a robust technique that does not suffer from the  $180^\circ$ -transfer difficulty of most Lambert routines [12].

## 3 NUMERICAL RESULTS

The methodology described in Section 2 has been applied considering two sensors moving on the same orbit and varying their separation in true anomaly (see subsection 3.1), varying the measurements uncertainties (see subsection 3.2), and varying the target taken into account (see subsection 3.3). It should be underlined that, since multiple objects are present in the images provided by the optical sensors, it is necessary to detect and match the object of interest acquired by the different space-based sensors. Various works address this data association problem [22, 23]. For the sake of simplicity, it has been assumed that both sensors have the task of observing the object of interest and that data association have already been performed.

### 3.1 Test case 1

In this subsection, the effect of varying the separation in the true anomaly has been analysed. Tab. 1 shows the orbital parameters of the two sensors examined. Specifically, it was assumed that the sensors are moving on a 6 p.m. – 6 a.m. Sun-synchronous orbit, and that they are characterised by a  $\Delta v = 2^\circ$ . The target chosen is COSMOS 1275 DEB, which is on a similar orbital plane as the two sensors and has a semi-major axis that is about 190 km larger than that of the two sensors. The initial epoch selected for the analysis is 6 March 2025 13:55:06.

Table 1. Orbital parameters of the two sensors, when  $\Delta v = 2^\circ$ .

Orbital parameters	Sensor 1	Sensor 2
$a$ (km)	7178.14	7178.14
$e$	0	0
$i$ ( $^\circ$ )	81.4	81.4
$\Omega$ ( $^\circ$ )	257.3	257.3
$\omega$ ( $^\circ$ )	0	0
$\nu$ ( $^\circ$ )	0	2

By propagating the two sensors and the object of interest under Keplerian assumption and considering a simulation time of 48 hours, an observation window of 1232 seconds

is obtained. The right ascension and declination angles provided by the two sensors during this observation window enable to determine the  $x_t$ ,  $y_t$  and  $z_t$  coordinates of the target according to Eqs. 14-16 and the estimates of  $\sigma_{x_t}$ ,  $\sigma_{y_t}$  and  $\sigma_{z_t}$  according to Eqs. 18-19 and 22, respectively. In this case, the positions of the sensors are assumed to be known from on-board GNSS systems and, thus, the values of  $\sigma_{x_t}$ ,  $\sigma_{y_t}$  and  $\sigma_{z_t}$  are obtained considering  $\sigma_{pos} = 0.5 m$ . Moreover, the angular uncertainties taken into account are  $\sigma_\theta = 0.0022^\circ$  and  $\sigma_\phi = 0.0022^\circ$  as in [7]. Fig. 5 shows the trends of  $\sigma_{x_t}$ ,  $\sigma_{y_t}$ ,  $\sigma_{z_t}$  as well as the separation angle between the two sensors  $\theta_2 - \theta_1$ .

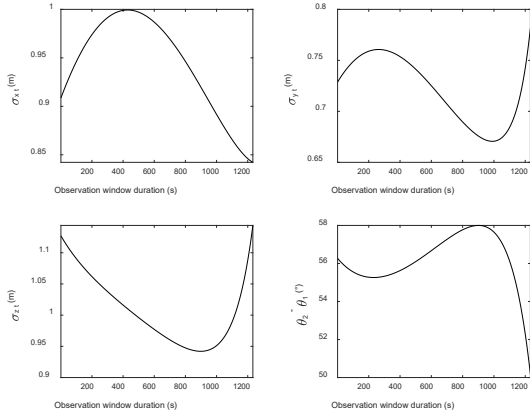


Figure 5. Trend of  $\sigma_{x_t}$ ,  $\sigma_{y_t}$ ,  $\sigma_{z_t}$  and  $\theta_2 - \theta_1$  during the observation window, when  $\Delta v = 2^\circ$ .

Tab. 2 provides the  $x_t$ ,  $y_t$  and  $z_t$  coordinates of the target and the estimates of  $\sigma_{x_t}$ ,  $\sigma_{y_t}$ , and  $\sigma_{z_t}$  obtained for the value of the separation angle closest to  $90^\circ$ , i.e.,  $\theta_2 - \theta_1 = 58.0^\circ$ .

Table 2.  $x_t$ ,  $y_t$  and  $z_t$  coordinates and  $\sigma_{x_t}$ ,  $\sigma_{y_t}$ , and  $\sigma_{z_t}$  for  $\theta_2 - \theta_1 = 58.0^\circ$ , when  $\Delta v = 2^\circ$ .

$x_t(km)$	1466.3
$y_t(km)$	2612.0
$z_t(km)$	6672.3
$\sigma_{x_t}(m)$	0.919
$\sigma_{y_t}(m)$	0.676
$\sigma_{z_t}(m)$	0.927

Tab. 3 gives the results of the IOD obtained by solving the Lambert's problem considering the two position vectors at the start and end of the observation window, i.e., 06-Mar-2025 20:54:56 and 06-Mar-2025 21:15:28, taking into account the corresponding uncertainties on the x, y and z coordinates.

Table 3. Results of the IOD, when  $\Delta v = 2^\circ$ .

Orbital parameters	True values	Estimated values	Percentage error (%)
$a$	7372.8 km	7372.8 km	$2.18 \times 10^{-5}$
$e$	0.0120	0.0120	$1.09 \times 10^{-3}$
$i$	$82.8^\circ$	$82.8^\circ$	$6.30 \times 10^{-6}$
$\Omega$	$257.0^\circ$	$257.0^\circ$	$1.56 \times 10^{-8}$
$\omega$	$64.5^\circ$	$64.5^\circ$	$3.51 \times 10^{-4}$
$\nu$	$356.1^\circ$	$356.1^\circ$	$6.67 \times 10^{-5}$

Then, the separation in true anomaly between the two sensors has been reduced to  $1^\circ$ . Therefore, the orbital parameters of the two sensors are the ones given in Tab. 1, but considering  $\nu = 1^\circ$  for the second sensor. By propagating the two sensors and the target of interest under Keplerian assumption for 48 hours, the two sensors can observe the target simultaneously for 1306 seconds, resulting in a longer observation window. Fig. 6 depicts the trends of  $\sigma_{x_t}$ ,  $\sigma_{y_t}$ ,  $\sigma_{z_t}$ , and  $\theta_2 - \theta_1$  during this observation window, considering  $\sigma_{pos} = 0.5 m$ ,  $\sigma_\theta = 0.0022^\circ$  and  $\sigma_\phi = 0.0022^\circ$ .

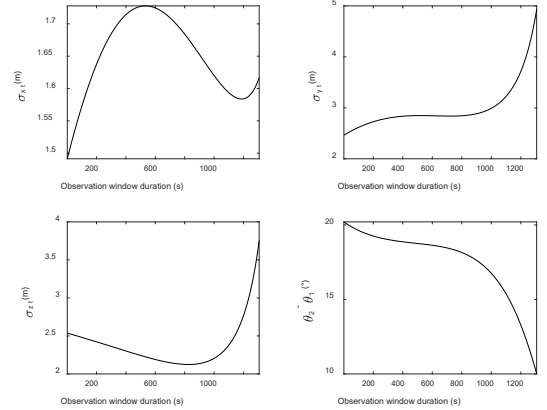


Figure 6. Trend of  $\sigma_{x_t}$ ,  $\sigma_{y_t}$ ,  $\sigma_{z_t}$  and  $\theta_2 - \theta_1$  during the observation window, when  $\Delta v = 1^\circ$ .

Tab. 4 reports the  $x_t$ ,  $y_t$  and  $z_t$  coordinates of the target and the estimates of  $\sigma_{x_t}$ ,  $\sigma_{y_t}$ , and  $\sigma_{z_t}$  derived for the value of the separation angle closest to  $90^\circ$ , i.e.,  $\theta_2 - \theta_1 = 20.2^\circ$ . It should be observed that the values of  $\sigma_{x_t}$ ,  $\sigma_{y_t}$ , and  $\sigma_{z_t}$  obtained for  $\Delta v = 1^\circ$  are greater by an order of magnitude than those obtained for  $\Delta v = 2^\circ$ . Indeed, when  $\Delta v$  decreases, the separation angles  $\theta_2 - \theta_1$  between the sensors also reduces, resulting in higher values of  $\sigma_{x_t}$ ,  $\sigma_{y_t}$ , and  $\sigma_{z_t}$ .

Table 4.  $x_t$ ,  $y_t$  and  $z_t$  coordinates and  $\sigma_{x_t}$ ,  $\sigma_{y_t}$ , and  $\sigma_{z_t}$  for  $\theta_2 - \theta_1 = 20.2^\circ$ , when  $\Delta v = 1^\circ$ .

$x_t(km)$	-26.4
$y_t(km)$	-3663.7
$z_t(km)$	6296.4
$\sigma_{x_t}(m)$	1.49
$\sigma_{y_t}(m)$	2.46
$\sigma_{z_t}(m)$	2.54

Tab. 5 presents the results of the IOD obtained by solving the Lambert's problem considering the two position vectors at the start and end of the observation window, i.e., 06-Mar-2025 20:54:56 and 06-Mar-2025 21:16:42, taking into account the corresponding uncertainties on the x, y and z coordinates. Note that the IOD accuracy reduces compared to the case of  $\Delta v = 2^\circ$  due to the higher values of  $\sigma_{x_t}$ ,  $\sigma_{y_t}$ , and  $\sigma_{z_t}$ .

Table 5. Results of the IOD, when  $\Delta v = 1^\circ$ .

Orbital parameters	True values	Estimated values	Percentage error (%)
$a$	7372.8 km	7372.8 km	$1.05 \times 10^{-04}$
$e$	0.0120	0.0120	$7.51 \times 10^{-03}$
$i$	$82.8^\circ$	$82.8^\circ$	$4.08 \times 10^{-06}$
$\Omega$	$257.0^\circ$	$257.0^\circ$	$1.27 \times 10^{-06}$
$\omega$	$64.5^\circ$	$64.5^\circ$	$8.89 \times 10^{-04}$
$\nu$	$356.1^\circ$	$356.1^\circ$	$1.69 \times 10^{-04}$

Finally, the separation in true anomaly between the two sensors has been increased to  $3^\circ$ . Therefore, the orbital parameters of the two sensors are the ones shown in Tab. 1, but considering  $\nu = 3^\circ$  for the second sensor. In this case, an observation window of 1044 seconds is obtained by propagating the two sensors and the target of interest under Keplerian assumption for 48 hours. Fig. 7 illustrates the trends of  $\sigma_{x_t}$ ,  $\sigma_{y_t}$ ,  $\sigma_{z_t}$ , and  $\theta_2 - \theta_1$  during this observation window, considering  $\sigma_{pos} = 0.5 m$ ,  $\sigma_\theta = 0.0022^\circ$  and  $\sigma_\phi = 0.0022^\circ$ . Note that the values of  $\sigma_{x_t}$ ,  $\sigma_{y_t}$  and  $\sigma_{z_t}$  obtained for  $\Delta v = 3^\circ$  are smaller than those obtained for  $\Delta v = 2^\circ$ , since the separation angles  $\theta_2 - \theta_1$  between sensors during the observation window are closer to  $90^\circ$  for the case of  $\Delta v = 3^\circ$  compared to the case of  $\Delta v = 2^\circ$ . Tab. 6 gives the estimates of  $x_t$ ,  $y_t$ ,  $z_t$ ,  $\sigma_{x_t}$ ,  $\sigma_{y_t}$ , and  $\sigma_{z_t}$  evaluated for the value of the separation angle closest to  $90^\circ$ , i.e.,  $\theta_2 - \theta_1 = 91.1^\circ$ . Tab. 7 provides the results obtained by solving the Lambert's problem considering the two position vectors at the start and end of the observation window, i.e., 06-Mar-2025

20:54:56 and 06-Mar-2025 21:12:20, taking into account the corresponding uncertainties on the x, y and z coordinates. In this case, the IOD accuracy is comparable to that obtained for  $\Delta v = 2^\circ$ .

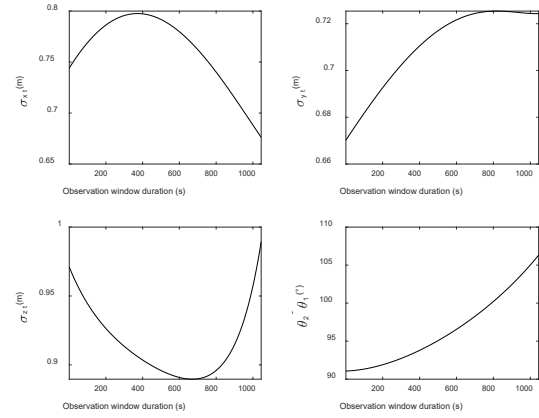


Figure 7. Trend of  $\sigma_{x_t}$ ,  $\sigma_{y_t}$ ,  $\sigma_{z_t}$  and  $\theta_2 - \theta_1$  during the observation window, when  $\Delta v = 3^\circ$ .

Table 6.  $x_t$ ,  $y_t$  and  $z_t$  coordinates and  $\sigma_{x_t}$ ,  $\sigma_{y_t}$ , and  $\sigma_{z_t}$  for  $\theta_2 - \theta_1 = 91.1^\circ$ , when  $\Delta v = 3^\circ$ .

$x_t(km)$	-26.4
$y_t(km)$	-3663.7
$z_t(km)$	6296.4
$\sigma_{x_t}(m)$	0.744
$\sigma_{y_t}(m)$	0.670
$\sigma_{z_t}(m)$	0.971

Table 7. Results of the IOD, when  $\Delta v = 3^\circ$ .

Orbital parameters	True values	Estimated values	Percentage error (%)
$a$	7372.8 km	7372.8 km	$2.06 \times 10^{-05}$
$e$	0.0120	0.0120	$1.10 \times 10^{-03}$
$i$	$82.8^\circ$	$82.8^\circ$	$4.50 \times 10^{-06}$
$\Omega$	$257.0^\circ$	$257.0^\circ$	$2.23 \times 10^{-07}$
$\omega$	$64.5^\circ$	$64.5^\circ$	$4.51 \times 10^{-04}$
$\nu$	$356.1^\circ$	$356.1^\circ$	$8.45 \times 10^{-05}$

To sum up, the following consideration can be made. Although a lower separation in true anomaly between the two sensors (i.e.,  $\Delta v = 1^\circ$ ) results in a longer observation window due to similar illumination conditions, the values of  $\sigma_{x_t}$ ,  $\sigma_{y_t}$  and  $\sigma_{z_t}$  become more significant as the separation angles between the sensors  $\theta_2 - \theta_1$  become

smaller. Conversely, a greater separation in the true anomaly (i.e.,  $\Delta v = 3^\circ$ ) results in separation angles between the sensors  $\theta_2 - \theta_1$  closer to  $90^\circ$ , leading to lower  $\sigma_{x_t}$ ,  $\sigma_{y_t}$  and  $\sigma_{z_t}$  values and, thus, a more accurate IOD.

### 3.2 Test case 2

In this subsection, the effect of varying the measurements uncertainties has been examined. This analysis has been performed considering the sensors given in Tab. 1 and selecting COSMOS 1275 DEB as target of interest.

First, it is assumed that the positioning uncertainty resembles the order of magnitude of TLE-based information. Therefore, in this case, it is assumed that  $\sigma_{pos} = 1000$  m, while the values considered for the angular uncertainties are  $\sigma_\theta = 0.0022^\circ$  and  $\sigma_\phi = 0.0022^\circ$ . In this case, the trends of  $\sigma_{x_t}$ ,  $\sigma_{y_t}$ ,  $\sigma_{z_t}$ , as well as the separation angle between the two sensors  $\theta_2 - \theta_1$ , are depicted in Fig. 8. Tab. 8 provides the values of  $x_t$ ,  $y_t$ ,  $z_t$ ,  $\sigma_{x_t}$ ,  $\sigma_{y_t}$ , and  $\sigma_{z_t}$  obtained for the value of the separation angle closest to  $90^\circ$ , i.e.,  $\theta_2 - \theta_1 = 58.0^\circ$ . Tab. 9 gives the results obtained by solving the Lambert's problem, considering the two position vectors at the start and end of the observation window, i.e., 06-Mar-2025 20:54:56 and 06-Mar-2025 21:15:28, and taking into account the corresponding uncertainties on the x, y and z coordinates. When sensor positions are assumed to be known from the TLEs, the accuracy of the IOD results decreases significantly for the semi-major axis, eccentricity, argument of perigee and true anomaly, although reasonable accuracy is still retained. The inclination and right ascension of the ascending node values also degrade, although they are the orbital parameters estimated with the greatest accuracy (as occurs in the previous cases).

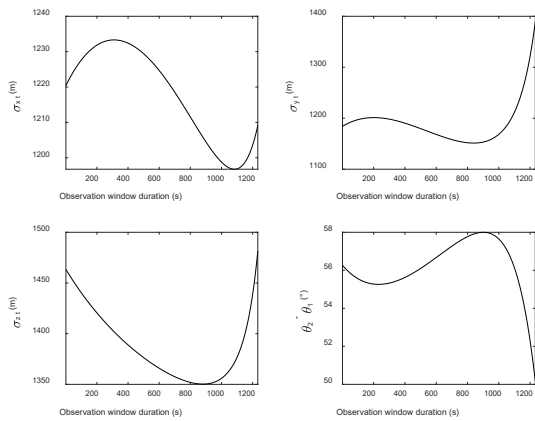


Figure 8. Trend of  $\sigma_{x_t}$ ,  $\sigma_{y_t}$ ,  $\sigma_{z_t}$  and  $\theta_2 - \theta_1$  during the observation window, when  $\sigma_{pos} = 1000$  m,  $\sigma_\theta = 0.0022^\circ$  and  $\sigma_\phi = 0.0022^\circ$ .

Table 8.  $x_t$ ,  $y_t$  and  $z_t$  coordinates and  $\sigma_{x_t}$ ,  $\sigma_{y_t}$ , and  $\sigma_{z_t}$  for  $\theta_2 - \theta_1 = 58.0^\circ$ , when  $\sigma_{pos} = 1000$  m,  $\sigma_\theta = 0.0022^\circ$  and  $\sigma_\phi = 0.0022^\circ$ .

$x_t$ (km)	1466.3
$y_t$ (km)	2612.0
$z_t$ (km)	6672.3
$\sigma_{x_t}$ (m)	1204.4
$\sigma_{y_t}$ (m)	1153.3
$\sigma_{z_t}$ (m)	1350.4

Table 9. Results of the IOD, when  $\sigma_{pos} = 1000$  m,  $\sigma_\theta = 0.0022^\circ$  and  $\sigma_\phi = 0.0022^\circ$ .

Orbital parameters	True values	Estimated values	Percentage error (%)
$a$	7372.8 km	7375.2 km	0.0323
$e$	0.0120	0.0122	1.87
$i$	$82.8^\circ$	$82.8^\circ$	0.00822
$\Omega$	$257.0^\circ$	$257.0^\circ$	$1.34 \times 10^{-4}$
$\omega$	$64.5^\circ$	$64.2^\circ$	0.588
$v$	$356.1^\circ$	$356.5^\circ$	0.111

Then, the case in which the accuracy of the angular measurements degrades by an order of magnitude has been analysed. Assuming that the positioning uncertainty of the sensors is consistent with the order of magnitude of GNSS-based orbit determination in LEO, it has been considered that  $\sigma_{pos} = 0.5$  m,  $\sigma_\theta = 0.022^\circ$  and  $\sigma_\phi = 0.022^\circ$ . The trends of  $\sigma_{x_t}$ ,  $\sigma_{y_t}$ ,  $\sigma_{z_t}$  as well as the separation angle between the two sensors  $\theta_2 - \theta_1$  are illustrated in Fig. 9. Tab. 10 gives the values of  $x_t$ ,  $y_t$ ,  $z_t$ ,  $\sigma_{x_t}$ ,  $\sigma_{y_t}$ , and  $\sigma_{z_t}$  obtained for  $\theta_2 - \theta_1 = 58.0^\circ$ . Note that, when considering  $\sigma_\theta = 0.022^\circ$  and  $\sigma_\phi = 0.022^\circ$ , the values of  $\sigma_{x_t}$ ,  $\sigma_{y_t}$ , and  $\sigma_{z_t}$  by an order of magnitude compared to the case of  $\sigma_\theta = 0.0022^\circ$  and  $\sigma_\phi = 0.0022^\circ$ . Tab. 11 reports the results obtained by solving the Lambert's problem, considering the two position vectors at the start and end of the observation window, i.e., 06-Mar-2025 20:54:56 and 06-Mar-2025 21:15:28, and taking into account the corresponding uncertainties on the x, y and z coordinates. The results of IOD are still good, although the accuracy with which orbital parameters are calculated is reduced by an order of magnitude. This is particularly true for inclination and right ascension, which are the most accurately estimated orbital parameters.

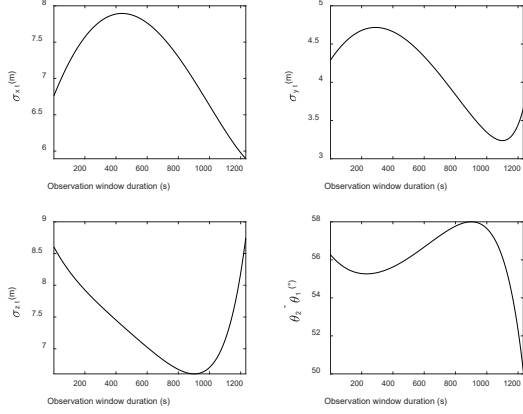


Figure 9. Trend of  $\sigma_{x_t}$ ,  $\sigma_{y_t}$ ,  $\sigma_{z_t}$  and  $\theta_2 - \theta_1$  during the observation window, when  $\sigma_{pos} = 0.5$  m,  $\sigma_\theta = 0.022^\circ$  and  $\sigma_\phi = 0.022^\circ$ .

Table 10.  $x_t$ ,  $y_t$  and  $z_t$  coordinates and  $\sigma_{x_t}$ ,  $\sigma_{y_t}$ , and  $\sigma_{z_t}$  for  $\theta_2 - \theta_1 = 58.0^\circ$ , when  $\sigma_{pos} = 0.5$  m,  $\sigma_\theta = 0.022^\circ$  and  $\sigma_\phi = 0.022^\circ$ .

$x_t$ (km)	1466.3
$y_t$ (km)	2612.0
$z_t$ (km)	6672.3
$\sigma_{x_t}$ (m)	6.97
$\sigma_{y_t}$ (m)	3.57
$\sigma_{z_t}$ (m)	6.60

Table 11. Results of the IOD, when  $\sigma_{pos} = 0.5$  m,  $\sigma_\theta = 0.022^\circ$  and  $\sigma_\phi = 0.022^\circ$ .

Orbital parameters	True values	Estimated values	Percentage error (%)
$a$	7372.8 km	7372.8 km	$1.39 \times 10^{-04}$
$e$	0.0120	0.0120	0.00534
$i$	$82.8^\circ$	$82.8^\circ$	$4.88 \times 10^{-05}$
$\Omega$	$257.0^\circ$	$257.0^\circ$	$1.65 \times 10^{-07}$
$\omega$	$64.5^\circ$	$64.5^\circ$	0.00207
$\nu$	$356.1^\circ$	$356.1^\circ$	$3.96 \times 10^{-04}$

### 3.3 Test case 3

This subsection presents the results obtained by selecting PEGASUS DEB as the target of interest. Its orbit plane is similar to that of the two sensors, with a semi-major axis approximately 180 km smaller. The sensors considered to perform this analysis are those shown in Tab. 1 while the selected initial epoch is 06-Mar-2025

07:01:02. In the present case, by propagating the sensors and the target under Keplerian assumption for 48 hours, the four observation windows given in Tab. 12 are obtained. In this case, the observation duration is increased because the time during which the Sun is in the sensors' field of view decreases.

Table 12. Observation windows considering PEGASUS DEB as target.

Window #	Duration (s)
1	2099
2	1648
3	2334
4	372

Fig. 10 shows the trends of  $\sigma_{x_t}$ ,  $\sigma_{y_t}$ ,  $\sigma_{z_t}$  obtained considering  $\sigma_{pos} = 0.5$  m,  $\sigma_\theta = 0.0022^\circ$  as well as the separation angle between the two sensors  $\theta_2 - \theta_1$ . It can be seen that  $\sigma_{x_t}$ ,  $\sigma_{y_t}$ , and  $\sigma_{z_t}$  reach very high values when the separation angle between the sensors is close to  $0^\circ$ .

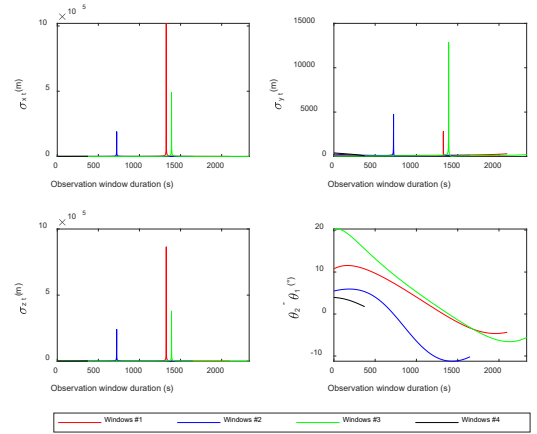


Figure 10. Trend of  $\sigma_{x_t}$ ,  $\sigma_{y_t}$ ,  $\sigma_{z_t}$  and  $\theta_2 - \theta_1$  during the observation window, considering PEGASUS DEB as target.

Tab. 13 provides the values of  $x_t$ ,  $y_t$ ,  $z_t$ ,  $\sigma_{x_t}$ ,  $\sigma_{y_t}$ , and  $\sigma_{z_t}$  obtained for the value of the separation angle closest to  $90^\circ$ , i.e.,  $\theta_2 - \theta_1 = 20.3^\circ$ , which is achieved during the third observation window. Note that the accuracy with which the target position is estimated is of the order of a few meters, since the maximum separation angle between the two sensors is relatively small. Tab. 14 gives the results obtained by solving the Lambert's problem, considering the two position vectors at the start and end of third observation window, i.e., 08-Mar-2025 03:11:19 and 08-Mar-2025 03:50:13, and taking into account the corresponding uncertainties on the x, y and z coordinates. It should be underlined that the determination of the

initial orbit has been carried out considering the third observation window as the values of  $\sigma_{x_t}$ ,  $\sigma_{y_t}$ , and  $\sigma_{z_t}$  at the start and end of that window are smaller.

Table 13.  $x_t$ ,  $y_t$  and  $z_t$  coordinates and  $\sigma_{x_t}$ ,  $\sigma_{y_t}$ , and  $\sigma_{z_t}$  for  $\theta_2 - \theta_1 = 20.3^\circ$ , considering PEGASUS DEB as target.

$x_t$ (km)	1115.4
$y_t$ (km)	1555.0
$z_t$ (km)	6753.2
$\sigma_{x_t}$ (m)	2.76
$\sigma_{y_t}$ (m)	3.91
$\sigma_{z_t}$ (m)	2.96

Table 14. Results of the IOD, considering PEGASUS DEB as target.

Orbital parameters	True values	Estimated values	Percentage error (%)
$a$	7000.8 km	7000.8 km	$6.31 \times 10^{-5}$
$e$	0.0115	0.0115	0.0149
$i$	$81.9^\circ$	$81.9^\circ$	$3.34 \times 10^{-5}$
$\Omega$	$264.7^\circ$	$264.7^\circ$	$7.89 \times 10^{-5}$
$\omega$	$359.8^\circ$	$359.8^\circ$	0.0013
$\nu$	$101.5^\circ$	$101.5^\circ$	0.0045

#### 4 CONCLUSIONS

This work investigated the feasibility of using space-based optical sensors to improve the 3D position and orbit estimation of an RSO of interest. First, the observation windows during which the object of interest can be observed by both sensors are determined. The observation windows have been determined assuming that the sensors are able to track the object of interest and considering observation constraints, such as the Earth's shadow, the Sun illumination, the presence of the Earth in the background and the target's visual magnitude. Then, the simultaneous angular measurements obtained during the observation windows have been used to determine the 3D location of an RSO of interest by applying a state-of-the-art triangulation method. The obtained range information has been exploited to improve the accuracy of IOD by transforming the angles-only IOD problem into IOD with 3D position data. In particular, the initial orbit of the RSO of interest has been determined by solving the Lambert problem using the Battin's method. A sensitivity analysis has been carried out to assess how the true anomaly separation between

the sensors and uncertainties on the angular measurements provided by the sensors and on sensor positions affect the accuracy with which the 3D position of the object of interest and its initial orbit is determined. The results showed that when the separation in true anomaly between the sensors is relatively small (i.e.,  $\Delta\nu = 1^\circ$ ), the accuracy with which the initial orbit and 3D position of the object is determined is reduced compared to the case of a larger separation in true anomaly (i.e.,  $\Delta\nu = 2^\circ$  and  $\Delta\nu = 3^\circ$ ). Furthermore, when sensor positions are assumed to be consistent with TLE and not with on-board GNSS receiver performance in LEO (i.e.,  $\sigma_{pos} = 1000$  m instead of  $\sigma_{pos} = 0.5$  m), the accuracy of IOD results is significantly degraded, although the accuracy with which the inclination and right ascension of the ascending node is estimated is quite good compared to that of the other orbital parameters. Conversely, when considering degraded angular measurements (i.e.,  $\sigma_\theta$  and  $\sigma_\phi$  of the order of  $10^{-2}$  degrees instead of  $10^{-3}$  degrees), the accuracy of IOD decreases, while still remaining good. Future works could investigate different geometric configurations between sensors, also considering cross-track separations, and examining how the accuracy of range and IOD estimation changes in these cases. In addition, insights can be given into the real-world applicability of this technique by performing a more comprehensive analysis.

#### 5 ACKNOWLEDGEMENTS

This work has been developed within the project "Attività tecnico-scientifiche di supporto a C-SSA/ISOC e simulazione di architetture di sensori per SST" funded by the Italian Space Agency (ASI).

#### 6 REFERENCES

1. ESA. (2024). *ESA Space Environment Report 2024*.
2. H. Yunpeng, L. Kebo, L. Yan'Gang, & C. Lei. (2021). Review on strategies of space-based optical space situational awareness. *Journal of Systems Engineering and Electronics* 32(5) 1152–1166.
3. L. Felicetti, & M.R. Emami. (2016). A multi-spacecraft formation approach to space debris surveillance. *Acta Astronautica* 127 491–504.
4. E. Gaposchkin, C. Braun, & J. Sharma. (2000). Space-Based Space Surveillance with the Space-Based Visible. *Journal of Guidance Control and Dynamics* 23 148–152.
5. J. Utzmann, A. Wagner, J. Silha, T. Schildknecht, P. Willemsen, F. Teston, & T. Flohrer. (2014). A system design for space-based space surveillance. In *Proceedings of Small Satellites Systems & Services Symposium*, Porto Petro.

6. A. Scott, J. Hackett, & K. Man. (2013). On-Orbit Results for Canada's Sapphire Optical Payload. In *Advanced Maui Optical and Space Surveillance Technologies Conference*, Maui, Hawaii, USA.
7. K. Hussain, K. Thangavel, A. Gardi, & R. Sabatini. (2023). Passive Electro-Optical Tracking of Resident Space Objects for Distributed Satellite Systems Autonomous Navigation. *Remote Sensing* 15 1714.
8. A. Bernard, A.M. Nafi, & D. Geller. (2018). Using Triangulation in Optical Orbit Determination. In *AAS/AIAA Astrodynamics Specialist Conference*, Snowbird, Utah, USA.
9. L. Chen, C. Liu, Z. Li, & Z. Kang. (2021). A New Triangulation Algorithm for Positioning Space Debris. *Remote Sensing* 13 4878.
10. P. Vasudhara, W. Vongsantivanich, P. Jantawichayasuit, & S. Chaimatanan. (2022). Initial Orbit Determination for Space Situational Awareness System using Triangulation Method. In *2022 International Conference on Electrical, Computer and Energy Technologies (ICECET)*.
11. J. Sanders-Reed. (2002). Triangulation Position Error Analysis for Closely Spaced Imagers. *SAE Technical Papers*.
12. D. Vallado. (2013). *Fundamentals of Astrodynamics and Applications*, Microcosm Press.
13. J. Shell. (2011). Commercially-Hosted Payloads for Debris Monitoring and Mission Assurance in GEO.
14. J. Sanders-Reed. (2001). Error propagation in two-sensor three-dimensional position estimation. *Optical Engineering* 40.
15. J.W. Gibbs. (1889). *On the Determination of Elliptical Orbits from Three Complete Observations*, Memoires National Academy of Science.
16. S. Herrick. (1971). *Astrodynamics: Orbit Determination, Space Navigation, Celestial Mechanics*, Van Nostrand Reinhold Co., London.
17. J.L. Lagrange. (1788). *Mecanique Analytique*, Académie des Sciences, Paris.
18. C.F. Gauss. (1857). *Theory of the motion of the heavenly bodies moving about the Sun in conic sections: a translation of Carl Frdr. Gauss Theoria motus.*, Brown and Co.
19. R.H. Battin. (1999). *An Introduction to the Mathematics and Methods of Astrodynamics*, AIAA Education Series, New York.
20. R.H. Gooding. (1990). A procedure for the solution of Lambert's orbital boundary-value problem. *Celestial Mechanics and Dynamical Astronomy* 48(2) 145–165.
21. J.D. and B.R.D. Thorne. (1995). Series Reversion/Inversion of Lambert's Time Function. *Journal of the Astronautical Sciences* 43(3) 277–287.
22. B. Reihs, A. Vananti, J. Siminski, T. Flohrer, & T. Schildknecht. (2019). *Analysing the Correlation Performance of ESA's Planned Space-based GEO Surveillance Mission*.
23. X. Lei, K. Wang, P. Zhang, T. Pan, H. Li, J. Sang, & D. He. (2018). A geometrical approach to association of space-based very short-arc LEO tracks. *Advances in Space Research* 62(3) 542–553.